Journal of Atmospheric and Solar-Terrestrial Physics 72 (2010) 1008–1018

Contents lists available at ScienceDirect

Journal of Atmospheric and Solar-Terrestrial Physics

journal homepage: www.elsevier.com/locate/jastp

The statistical and numerical study of the global distribution of coronal plasma and magnetic field near 2.5 Rs over a 10-year period

Fang Shen*, Xueshang Feng, Changqing Xiang, Wenbin Song

State Key Laboratory of Space Weather, Center for Space Science and Applied Research, Chinese Academy of Sciences, Beijing 100190, China

ARTICLE INFO

Article history:
Received 1 February 2010
Received in revised form
28 May 2010
Accepted 28 May 2010
Available online 4 June 2010

Keywords:
Global coronal plasma and field distribution
Coronal mass outputs flux

ABSTRACT

The basic characteristics of the global distribution for the corona plasma and magnetic field near 2.5 Rs are analyzed with the statistical and numerical methods for 136 Carrington Rotations (CRs) covering four different phases of solar activity. By using the observational data and the velocity distribution model in the corona, the statistical average distribution of the magnetic field, density and the coronal mass outputs are analyzed for the four different phases. Then, a numerical study of the global distribution near 2.5 Rs has been made by solving a self-consistent MHD system. Finally, the solar wind speed at 1 AU is given by mapping the speed at 2.5 Rs to that near 1 AU, and the comparison of the numerical results with the observational measurements and the simulation result of the Wang–Sheeley–Arge (WSA) model are made during more than 5 years. The numerical results indicate that the global distributions on the source surface of 2.5 Rs at different phases of solar activity could be used to predict the change of the solar wind in interplanetary space.

© 2010 Elsevier Ltd. All rights reserved.

1. Introduction

The study of the global distribution of magnetic structures and plasma properties (such as density, temperature, velocity field and coronal mass outputs) in the heliosphere is an important topic in determining the initial boundary conditions of constructing three-dimensional (3D) structures near the Sun and in the heliosphere (Priest et al., 1998), and further it could improve space weather prediction accuracy (Dryer, 1994; Guo and Wu, 1998). At present, although in-situ observations near the Sun are not available due to the limitations of space measurements, some progress in this topic has still been made (Odstrcil et al., 2004; Owens et al., 2008; Hu et al., 2008).

The solar magnetic field structures and coronal mass outputs in the heliosphere have a close relationship with the solar magnetic field (Wei et al., 2003). It is well known that the structures of the Sun's photospheric magnetic field vary systematically over a period of about 11 years in relation to the solar activity cycle, and the four phases of a solar cycle can be identified: maximum, descending phase, minimum and ascending phase. Near the solar minimum, a dipole pattern dominates the large-scale structure of the solar corona, while long-lived helmet streamers and large polar coronal holes can persist over several solar rotations. On the other hand, at the solar maximum, higher order components of the magnetic field can be as large as or larger than the dipole term, and the presence of many small-scale active regions further complicate the structure in the heliosphere (Linker et al., 1999; Riley et al., 2006; Hu et al., 2008). A physically important structure in the heliosphere is the heliospheric current sheet (HCS), which separates the magnetic field lines originating from opposite hemispheres. The shape and location of the HCS can also vary remarkably in relation to the solar cycle, which has a significant influence on the evolution of the interplanetary disturbances as well as on the modulation of galactic cosmic rays (Feng and Zhao, 2006; Smith, 2001; Hu et al., 2008). The solar surface magnetic field plays a crucial role in determining the structure of the solar corona and inner heliosphere (Linker et al., 1999). Different models of the global solar corona have been developed in the last several decades, based on the increasing ground- and space-based observations of the photospheric magnetic field (Riley et al., 2006). The global coronal magnetic structure was described by using a MHD model and an observed line-of-sight photospheric magnetic field from the Wilcox Solar Observatory (WSO) as boundary conditions (Hu et al., 2008). Their results illustrated how the shape and location of the HCS and the coronal magnetic field configuration evolved during the course of a solar cycle.

Based on the global distribution of the solar magnetic field, the basic characteristics of the coronal mass output (F_m) near the Sun could be analyzed with statistical and numerical methods by

* Corresponding author. Tel.: +8610 62586353.
E-mail addresses: fshen@spaceweather.ac.cn (F. Shen), fengx@spaceweather.ac.cn (X. Feng), cqxiang@spaceweather.ac.cn (C. Xiang), wbsong@spaceweather.ac.cn (W. Song).

1364-6826/$ - see front matter © 2010 Elsevier Ltd. All rights reserved.
doi:10.1016/j.jastp.2010.05.016

using observational data from K corona brightness, interplanetary scintillation and photospheric magnetic field (Wei et al., 2003). Their research showed that the highest and the lowest F_m were associated with the coronal current sheet and the polar corona regions, respectively, and the other regions were associated with a moderate F_m during the descending phase (1983), and the minimum (1984) of solar activity. In the study of a solar wind model, Withbroe (1988) took a mean value from Lallement et al. (1986) and Withbroe et al. (1985), which gives $N_p v = 2.3 \times 10^8$/ cm^2 (s), as an empirical constraint for the partial flux of a high-speed wind near the ecliptic plane at 1 AU and also deduced that F_m in the polar coronal region was about one half of F_m from other regions at 1 AU.

More and more authors realized the importance of understanding the relation among the solar wind speed, the coronal magnetic structures, and the coronal holes. Neugebauer et al. (1998) mapped the solar wind speed observed by Ulysses to the source surface of 2.5 Rs and compared it with the coronal hole structure. Their results showed that the highest speed wind came from the polar coronal holes, with the wind originating deeper within the holes being faster than the wind coming from near the holes' boundary. Fisk (2001) considered processes that should have resulted in motions of the magnetic field in the quasi-steady polar coronal holes near solar minimum, where he used the following three assumptions: (1) the solar wind that flows along the magnetic field from the polar coronal hole undergo a nonradial expansion; (2) the nonradial expansion is not centered on the rotation axis of the Sun; (3) the magnetic field is anchored in the differentially rotating photosphere. He also concluded that the interaction between the differential rotation of the photosphere and the nonradial expansion of the solar wind in the corona can lead to a large scale, systematic motion of coronal magnetic fields and could influence the structure of the heliospheric magnetic field. However, to seek observational evidence in support of this model from magnetic field data in the heliosphere is a difficult task. Recently, Scholl and Habbal (2008) presented a new method for the automated detection and classification of coronal holes based on EUV and magnetogram observations of the solar disk. They found that coronal holes had a skewed distribution of magnetic-field intensities, with values often reaching 100–200 G, and a relative magnetic-flux imbalance. All of the results mentioned above imply that the evolution (or motions) of the magnetic field structure on the photosphere could play an important role in controlling the magnetic structures in the corona and even in the heliosphere.

The numerical MHD model (Linker et al., 1999; Riley et al., 2001) has also been used for understanding the global picture of the solar corona and heliosphere for the "Whole Sun Month". The large-scale structure of solar wind observed by Ulysses near solar minimum was also simulated by Feng et al. (2005) using a 3D MHD regional combination numerical model (hereafter called Corona-interplanetary TVD MHD model—COIN-TVD model for brevity). On the basis of the observations of the solar photospheric magnetic field together with additional volumetric heating and momentum (Suess et al., 1996; Wang et al., 1998) to MHD equations, the large-scale bimodal solar wind (i.e., fast and slow wind) structure mentioned above was reproduced by using a 3D MHD model, and their numerical results were approximately consistent with Ulysses' observations. Their simulation showed that the initial magnetic field topology and the addition of volume heating could govern the bimodal structure of the solar wind observed by Ulysses and also demonstrated that the 3D MHD numerical model used by them was efficient in modeling the large-scale solar wind structure. Shen et al. (2007) also used a 3D time-dependent, COIN-TVD model to obtain the background solar wind from the source surface of 2.5 Rs to the Earth's orbit (215 Rs) and beyond. Based on the observations of the solar magnetic field and K-coronal brightness, Shen et al. (2007) established a self-consistent structure on the source surface as the inner boundary condition. Riley et al. (2001) and Linker et al. (1999) have developed an empirical procedure to drive global MHD model of the solar corona and inner heliosphere. Their procedure was to use the output of the coronal solution directly to provide the inner boundary condition of the heliospheric model. In modeling the solar corona they specified at the lower boundary the radial component of the magnetic field B_r based on the observed line-of-sight measurements of the photospheric magnetic field. Uniform characteristic values were used for the plasma density and temperature. Initial estimates of the field and plasma parameters were found from a potential field model and a Parker (1963) transonic solar wind solution, respectively. Their results showed that the simulations reproduced the overall large-scale features of the observations during the "Whole Sun Month" (August/September 1996), although the specified lower boundary conditions were very primitive.

Using the observed solar cycle dependent and self-consistent lower boundary conditions, on the basis of observation results, will play a very important role for the construction of a 3D background solar wind numerical model; however, the knowledge of the global distributions of the various coronal parameters on the source surface (2.5 Rs) near the Sun during different phases of solar activities are not sufficient for a quantitative study. By solving the self-consistent MHD system based on the observations of K coronal brightness and the photospheric magnetic fields, Wei et al. (2003) have made a preliminary test study of the global distribution near 2.5 Rs for Carrington Rotation (CR) 1742 in 1983 (at descending phase). The purpose of the present paper is to analyze the basic characteristics of the global distribution on the source surface (2.5 Rs) with statistical and numerical methods spanning all phases of solar activity. The main difficulties are that the global observations of velocity, temperature and magnetic field in the solar atmosphere are very limited (Wei et al., 2003), and the structures of the solar magnetic field are quite different at different phases in relation to the solar activity cycle (Hu et al., 2008). Because of these difficulties, we make a qualitative statistical analysis from the limited observations of the photospheric magnetic fields and K coronal brightness for 136 CRs covering the four different phases of solar activity to obtain information on the source surface of 2.5 Rs. Then, we carry out a numerical study to get the self-consistent global distribution of the various physical parameters on the source surface suitable for the different phases of solar activity, based on statistical analysis. Finally, we obtain the solar wind speed at 1 AU by mapping the speed from the source surface of 2.5 Rs to that near 1 AU, which leads to a more quantitative initial-boundary condition in numerical models of space weather events such as carried out by Shen et al. (2007).

2. Statistical research

The present study selects a time interval of 136 CRs, which span the period from January 1989 to March 1999. The selected CRs can be broadly grouped into following four categories according to the solar activity: (1)the solar maximum, CRs 1811–1825 (from January 1989 to February 1990), during the middle portion of solar cycle 22; (2) the descending phase, CRs 1826–1904 (from February 1990 to January 1996), during the latter portion of solar cycle 22; (3) the solar minimum, CRs 1905–1925 (from January 1996 to August 1997), during the final portion of solar cycle 22 and the early portion of solar cycle 23; (4) the ascending phase, CRs 1926–1946 (from August 1997 to March

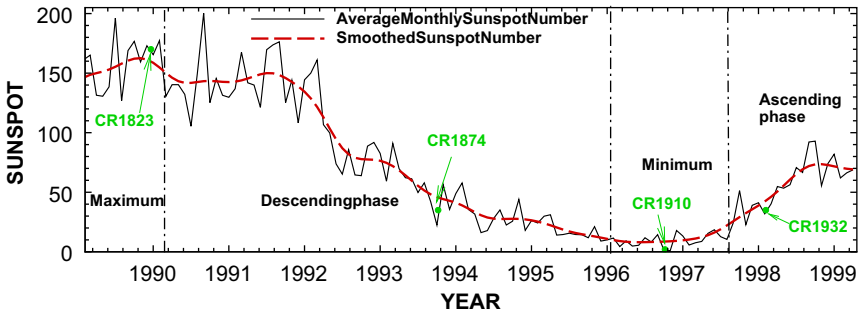

Fig. 1. The distributions of the average monthly (black solid line) and smoothed (red dashed line) number of sunspots from January 1989 to March 1999. The divisions of the four different phases are obvious in this figure, which are the maximum, from January 1989 to February 1990; the descending phase, from February 1990 to January 1996; the minimum, from January 1996 to August 1997; the ascending phase, from August 1997 to March 1999.

1999), during the early phase of solar cycle 23 (Oliver and Ballester, 1995; Harvey and White, 1999; Toma et al., 2000). Fig. 1 shows the distribution of the average monthly (black solid line) and smoothed (red dashed line) sunspot number from January 1989 to March 1999, and the four different phases of solar activity are marked by the dashed-dot line in the Fig. 1.

Line-of-sight (los) photospheric field (B_{los}) measurements have been made at the Wilcox Solar Observatory (WSO) at Stanford University since 1976, and are currently available on the web site http://wso.stanford.edu. Due to the line saturation effects, the observed magnetic field strength needs to be modified by a correction factor. Based on the calibration analysis of WSO and other solar observatories (Svalgaard et al., 1978; Svalgaard, 2006), a saturation factor of 1.8 is chosen for the observed data correction at WSO. Assuming that the magnetic field is truly radial in the region of the photosphere where the measurements are taken, the radial magnetic field B_r is specified at the inner boundary $r=1$ Rs by the relationship $B_r=B_{los}/\cos\theta$, where θ is the colatitude measured from the solar north pole (Wang and Sheeley, 1992; Luhmann et al., 2002). Then, assuming the radial magnetic field at 1 Rs to be the bottom boundary condition of the model of horizontal current and current sheet (HCCS) established by Zhao and Hoeksema (1994), we can determine the distributions of the radial magnetic field B_r on the source surface of 2.5 Rs for every CR. Fig. 2(a)–(d) gives the average global distributions of the radial magnetic field B_r on the source surface of 2.5 Rs over the four different phases of solar activity classified as above. It should be pointed out that the average is made every CR for the maximum (15 CRs), the minimum (21 CRs) and the ascending phase (21 CRs) and every four CRs (79 CRs) for the descending phase. Therefore, all the statistical averages are made through 15–21 rotations to get a statistically significant result and preserve the period of evolution information in the relatively long ascending phase.

The top four panels of Fig. 2 illustrate how the shape and location of the coronal current sheet and the coronal magnetic field configuration on the source surface of 2.5 Rs evolve during the course of the solar cycle. The current sheets are at the place $B_r=0$, which are represented by the green color in Fig. 2(a)–(d). We can easily see that the following: (1) at solar maximum (Fig. 2(a)), the current sheet becomes nearly vertical to the solar equator and displays its greatest complexity; (2) at the descending and ascending phases (Fig. 2(b) and (d)), the inclination of the current sheet is slightly large with respect to the equatorial plane; (3) at solar minimum (Fig. 2(c)), the current sheet at $r=2.5$ Rs is a flat line nearly in the solar equatorial plane with little spatial variability and small latitudinal excursion.

The inner coronal density here is derived from the K coronal polarized brightness (pB) by MKIII the High Altitude Observatory (HAO). Following the solar wind density model constructed by Guhathakurta et al. (1996), the corona density from 1 to 5.5 Rs is approximately expressed as follows (Xiang et al., 2006):

$$N(r,\theta,\varphi)=\begin{cases} N_{cs}\left[\dfrac{I_{pB}(r_0,\theta,\varphi)}{I_{pB_{cs}}}\right]^{1/2} & \text{(coronal streamer belt)} \\ N_h\left[\dfrac{I_{pB}(r_0,\theta,\varphi)}{I_{pB_h}}\right]^{1/2} & \text{(coronal hole region)} \\ N_h+(N_{cs}-N_h)e^{-4[I_{pB}(r_0,\theta,\varphi)-I_{pB_{cs}}/I_{pB_{cs}}+I_{pB_h}]^2} & \text{(other region)} \end{cases}$$

where (r,θ,φ) denoted the spherical coordinate system with its origin at the Sun's center. $r_0=1.36$ Rs, I_{pB} denotes the observation value of pB at 1.36 Rs, N_{cs} and N_h are the electron densities at the current sheet and the polar holes, which were expressed in detail by Guhathakurta et al. (1996).

Using the expression given by Xiang et al. (2006), the global density distribution at 2.5 Rs can be obtained for every CR. Fig. 2(e)–(h) shows the average number density distribution on the source surface during the same period as Fig. 2(a)–(d). The average of the density is also made every CR for the maximum (15 CRs), the minimum (21 CRs), and the ascending phase (21 CRs), and every four CRs (79 CRs) for the descending phase, which is same with that of B_r.

After getting the average distribution of the magnetic field and the number density at 2.5 Rs by observation, we will give the average global distribution of the coronal mass outputs at the source surface of 2.5 Rs.

Pätzold et al. (1997) employed the data obtained by Ulysses Solar Corona Experiment (SCE) during the first solar conjunction in summer 1991 to determine the electron density profiles in the streamer and the coronal hole. They found that the large-scale streamer belt electron density profile had a radial falloff exponent of -2.4 for distance greater than 7 Rs and that the acceleration terminates beyond 60 Rs, which was in agreement with Helios in-situ measurements. They also found that the coronal hole density profile had a radial falloff exponent of -3.94 beyond 5 Rs and that the acceleration termination radius should be in the range of 10–20 Rs, which was consistent with the conclusion that the acceleration termination radius for a polar coronal hole was at 10 Rs drawn from IPS observation by Grall et al. (1996). Based on these results, the coronal density of $r>5.5$ Rs could be obtained (Xiang et al., 2006). At the coronal hole and the quiet region, the acceleration termination radius is set as 10 Rs, and the density profile varied proportionally to $r^{-3.94}$; at the coronal streamer belt, the acceleration termination radius is set as far as over 100 Rs, and the density profile varied proportionally to $r^{-2.40}$. Thus, the distribution of the solar plasma density at 1 AU ($n(1\,\text{AU},\theta,\varphi)$) for the 136 CRs can be deduced based on the coronal density distribution at 2.5 Rs. Then, the solar wind speed

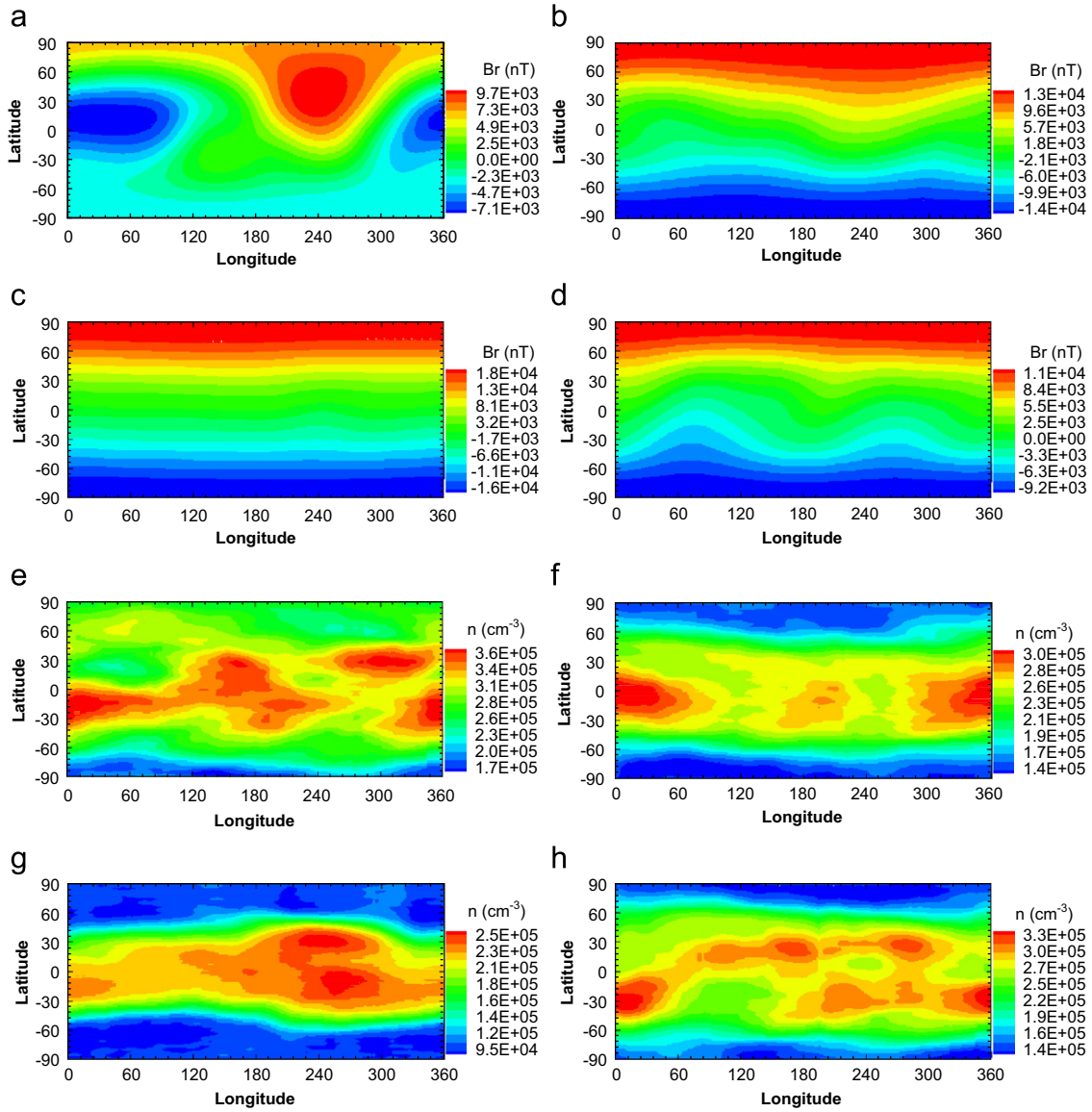

Fig. 2. The average distributions of the radial magnetic fields B_r and density over the four different phases: maximum, descending phase, minimum and ascending phase of solar activity as classified in Fig. 1.

at 1 AU and 2.5 Rs for every CR is derived through the observed density data, and the fact that the solar wind momentum flux density (F_μ) scaled to 1 AU is almost invariant except that it was slightly smaller in the latitude of $\pm 10^\circ \sim \pm 30^\circ$, which was given as $F_\mu(1\ \mathrm{AU},\theta,\varphi)=(1.05\sim 1.40)\times 10^{16}\ \mathrm{amu\ cm^{-1}\ s^{-2}}$ (Steinitz and Eyni, 1980; Mullan, 1983; Leinert and Jackson, 1998; Phillips et al., 1995; McComas et al., 2003). Once the radial solar wind speed at 1 AU is obtained by $v_r(1\ \mathrm{AU},\theta,\varphi)=[F_\mu(1\ \mathrm{AU},\theta,\varphi)\times 10^6/n(1\ \mathrm{AU},\theta,\varphi)]^{1/2}$, the radial solar wind speed at 2.5 Rs can be inferred from the conservation law of mass flux: $v_r(2.5\ \mathrm{Rs},\theta,\varphi)=(215\ \mathrm{Rs})^2 n(1\ \mathrm{AU},\theta,\varphi)v_r(1\ \mathrm{AU},\theta,\varphi)/[(2.5\ \mathrm{Rs})^2 n(2.5\ \mathrm{Rs},\theta,\varphi)]$ (Xiang et al., 2006). Fig. 3(a)–(d) gives the average radial solar speed distribution on the source surface over the four phases of solar activity.

Then, we can obtain the solar plasma mass flux, $F_m(2.5\ \mathrm{Rs},\theta,\varphi)=n(2.5\ \mathrm{Rs},\theta,\varphi)\ v(2.5\ \mathrm{Rs},\theta,\varphi)$, on the source surface according to the observations of the K coronal brightness and the solar plasma speed, where $n(2.5\ \mathrm{Rs},\theta,\varphi)$ and $v(2.5\ \mathrm{Rs},\theta,\varphi)$ denote the plasma density and the solar wind speed at 2.5 Rs, separately. Fig. 4(a)–(d) gives the average global distribution of F_m on the source surface over the four phases from the data in Figs. 2 and 3, where the various colors represent different mass flux intervals labeled at the right side of Fig. 4.

In Fig. 4, we can see that the larger area of flux output for $F_m > 1.8\times 10^{12}/\mathrm{cm^2\ s}$ at solar minimum (panel (c)) and for $F_m > 2.3\times 10^{12}/\mathrm{cm^2\ s}$ at the descending and ascending phase (panels (b) and (d)) are basically associated with the coronal current sheet regions in Fig. 2(c)–(d), respectively. Likewise, the smaller flux output for $F_m < 1.4\times 10^{12}/\mathrm{cm^2\ s}$ at solar minimum (panel (c)) and for $F_m < 1.5\times 10^{12}/\mathrm{cm^2\ s}$ at the descending and ascending phase (panels (b) and (d)) are basically associated with the polar coronal hole regions in Fig. 2(c)–(d), respectively. These characteristics of the coronal mass output are consistent with similar analysis made by Wei et al. (2003). However, from Figs. 2(a) and 4(a), no obvious correlation exists between the maximum F_m and the coronal current sheet patterns at the maximum. We also find in Fig. 4 that F_m basically is inclined to increase as the solar activity level increases. The four different

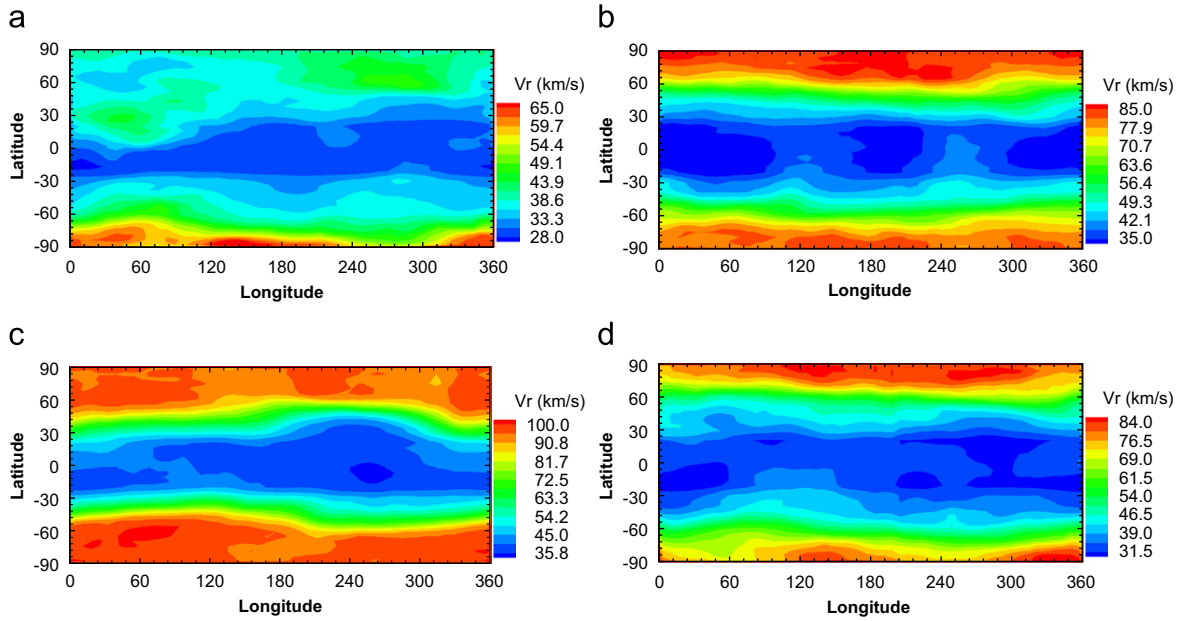

Fig. 3. The average distributions of the radial solar speed over the four different phases: maximum, descending phase, minimum and ascending phase of solar activity as classified in Fig. 1.

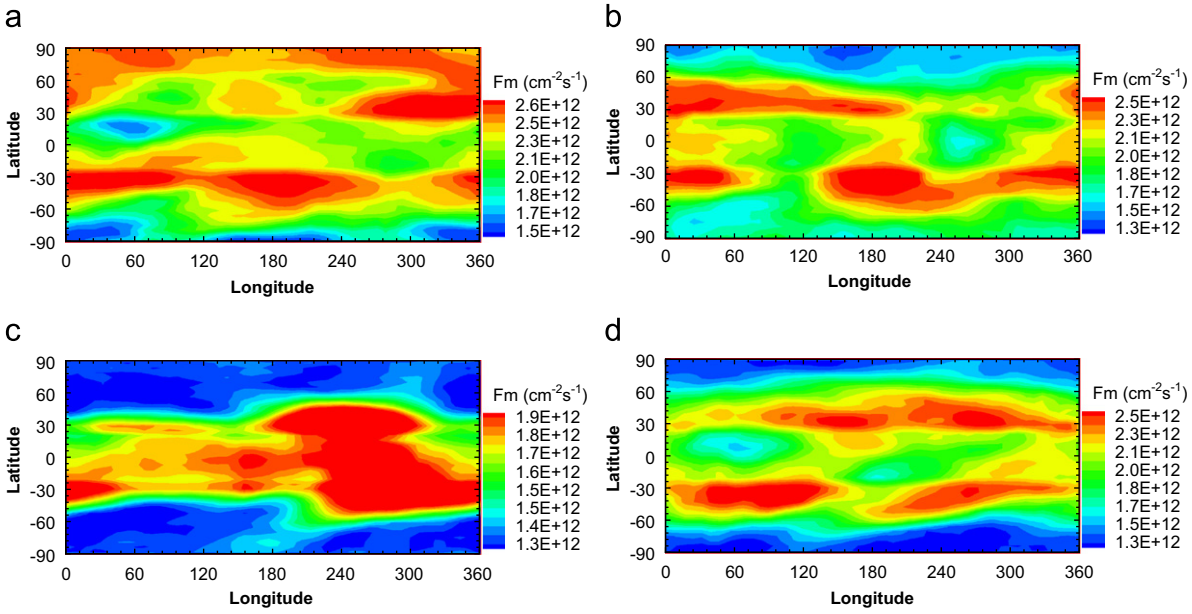

Fig. 4. The average distributions of coronal mass output F_m over the four different phases: maximum, descending phase, minimum, and ascending phase of solar activity.

distribution patterns of F_m(2.5 Rs,θ,φ) during the four phases of solar activity in Fig. 4 play a crucial role in the next section of our numerical study. In order to make sure that for every CR, the highest and the lowest F_m are associated with a coronal current sheet and the polar corona regions (Wei et al., 2003), we make a few corrections to the patterns of F_m(2.5 Rs,θ,φ) in Fig. 4, based on the different distribution characteristics of the solar magnetic field during each CR, which are expressed in detail in Section 3.

In this section, based on the observations of the photospheric magnetic fields and K coronal brightness on the source surface of 2.5 Rs for 136 CRs covering the four different phases of solar activity, the statistical average results of the magnetic field, the density and the coronal mass outputs flux pattern at 2.5 Rs were obtained for the four different phases of solar activity. These statistical average results of the coronal mass outputs flux F_m is fundamental for the numerical study in Section 3.

3. Numerical study

In this section we discuss a numerical study to give the solar cycle dependent, self-consistent global distribution of the various physical parameters on the source surface during all the phases of the solar cycle, based on the observation data of the magnetic field B, the density n and the statistical results of the coronal mass outputs flux F_m mentioned in the previous section. The ideal MHD equations are used for a qualitative study of F_m on the source surface, in which the assumption of the radial flow and magnetic field on the source

surface at 2.5 Rs is adopted as many authors used in making data analyses and numerical studies (e.g., Wang and Sheeley, 1990; Liewer et al., 2001; Wei et al., 2003). The one-dimensional (1D) MHD equations, that will be applied (Section 3) along each of the radii indicated by the grid points noted therein, are written as follows:

$$v\frac{\partial v}{\partial r}+n\frac{\partial v}{\partial r}+2nv/r=0, \tag{1}$$

$$nv\frac{\partial v}{\partial r}+\frac{\partial p}{\partial r}+ng=0, \tag{2}$$

$$n\frac{\partial p}{\partial r}-\gamma p\frac{\partial n}{\partial r}=0, \tag{3}$$

$$r\frac{\partial B}{\partial r}+2B=0, \tag{4}$$

$$p=2\Re nT, \tag{5}$$

$$\frac{\partial p}{\partial r}=2\Re' T\frac{\partial n}{\partial r}+2\Re' n\frac{\partial T}{\partial r}, \tag{6}$$

$$\beta(B)=8\pi p/B^2, \tag{7}$$

$$nv=F_{m_c}(2.5\mathrm{Rs},\theta,\varphi,B) \tag{8}$$

Here Eqs. (1)–(6) are well known (Wei et al., 2003), Eq. (7) is the statistical result for the plasma beta β. The plasma beta β variation with height in the solar atmosphere had been studied by Gary (2001). A model of the plasma beta β above an active region was presented by him and this model was representative and derived from a collection of sources. We can deduce from Fig. 3 of Gary (2001) that our statistical results for plasma beta β given by Eq. (7) are reasonable. Eq. (8) is the statistical distribution for the coronal mass outputs flux, which is based on the observational data of density and statistical result for $F_m(2.5\ \mathrm{Rs},\theta,\varphi)$ from Fig. 4. F_{m_c} is the correction made to F_m, whose purpose is to highlight the difference between F_m associated with the coronal current sheet and the polar corona regions (Wei et al., 2003).

Both Eqs. (7) and (8) are used for the closing condition of the MHD model and are expressed as follows:

$$\beta=\begin{cases}\beta_c & \text{(current sheet region)}\\ C/B^2 & \text{(other region)}\end{cases}$$

$$F_{m_c}(2.5\mathrm{Rs},\theta,\varphi,B)=\begin{cases}k_{n_c}F_m & (2.5\mathrm{Rs},\theta,\varphi) \quad \text{(current sheet region)}\\ k_{n_h}F_m & (2.5\mathrm{Rs},\theta,\varphi) \quad \text{(coronal hole region)}\\ k_{n_o}F_m & (2.5\mathrm{Rs},\theta,\varphi) \quad \text{(other region)}\end{cases}$$

Here,

$$k_{n_o}(B)=\begin{cases}1 & (B_l\le|B|<B_h)\\ k_{n_c}-(k_{n_c}-1)(B-B_c)/(B_l-B_c) & (|B|\le B_l)\end{cases}$$

where B_c and B_h are the magnetic field values near the current sheet region and at the boundaries of the coronal hole region, respectively. And $B_l=(1/3\text{–}2/3)B_h$ is the median value between B_c and B_h. $F_m(2.5\ \mathrm{Rs},\theta,\varphi)$ have four different distribution patterns over the four phases of solar activity as shown in Fig. 4.

The parameters involved here are $\gamma=1.4$. The other parameters β_c, C, k_{n_c} and k_{n_h} have different values in the four different phases of solar activity, which are expressed as follows:

(1) at the solar maximum: $\beta_c=7.5$, $C=0.75\times10^{-2}$ G^2, $k_{n_c}=1.7$ and $k_{n_h}=0.9$;
(2) at the descending and ascending phases: $\beta_c=1.5$, $C=0.45\times10^{-2}$ G^2, $k_{n_c}=1.5$ and $k_{n_h}=0.8$;
(3) at the solar minimum: $\beta_c=0.5$, $C=0.3\times10^{-2}$ G^2, $k_{n_c}=1.4$ and $k_{n_h}=0.9$.

The other 10 unknown parameters, B, $\partial B/\partial r$, v, $\partial v/\partial r$, T, $\partial T/\partial r$, n, $\partial n/\partial r$, p and $\partial p/\partial r$, can be found if any two of them are known by solving governing Eqs. (1)–(8). In the case investigated the magnetic field B and density n are two known inputs on the source surface at 2.5 Rs, which are given by statistical analyses. In the following computation, the source surface is divided into 182×92 cells with each being $2^\circ\times2^\circ$ in Carrington longitude and latitude respectively.

4. Numerical results and discussion

Based on the statistical average distributions of the radial magnetic field B_r, the numerical density n and the coronal mass flux F_{m_c} on source surface of 2.5 Rs, and the self-consistent MHD equations mentioned above, the numerical results of other parameters, such as temperature and radial velocity on the source surface can be deduced during every CR at solar maximum, the descending phase, solar minimum, and the ascending phase.

Four representative CRs corresponding to the four different phases, based on the sunspot distribution shown in Fig. 1 with green dot, are chosen to numerically generate the self-consistent, global distributions on the source surface at 2.5 Rs. Fig. 5 gives the numerical results of global distribution for the various physical parameters on the source surface during CR 1823 (at solar maximum, (i)), CR 1874 (at the descending phase, (ii)), CR 1910 (at solar minimum, (iii)) and CR 1932 (at the ascending phase, (iv)). In (i)–(iv) of Fig. 5, panels (a)–(e) describe the distribution of the radial magnetic field B_r, number density n from the observation, the correction result of the coronal mass output F_{m_c}, the numerical results of the temperature T, and radial velocity v_r, respectively.

From panel (c) of (i)–(iv) in Fig. 5, we find (1) at solar minimum, a good correlation exists between the maximum F_m and the coronal current sheet patterns (see the green area near $B_r=0$ in Fig. 5(iii)(a)); (2) at the descending and ascending phases, a distinguishable correlation exists between the maximum F_m and the coronal current sheet patterns (see the green area near $B_r=0$ in panel (a) of Fig. 5(ii) and (iv)); (3) at solar maximum, the correlation between the maximum F_m and the coronal current sheet patterns (see the green area near $B_r=0$ in Fig. 5(i)(a)) is irregular; (4) the minimum F_m in all the phases of solar activity, except at solar maximum, is associated with the polar corona region.

Panels (d), (e) from (i) to (iv) of Fig. 5 give the numerical results for the temperature and the radial velocity on the source surface during the different phases of solar activity. In all the phases, it is clear that the distributions of the temperature and speed on the source surface have complex structures. However, the distribution of the low-speed, low-temperature regions is basically consistent with the observed high-density regions and the current sheet regions. The high temperature and velocity regions, consistent with the low density regions, are located at the polar coronal hole regions. The regions where the temperature and velocity are too high are limited to the very small area of the polar coronal hole. (For example, at CR 1823 (the maximum, Fig. 5(i)), the region where the temperature is higher than 9×10^6 K and velocity is higher than 140 km/s.)

By examining the results of Fig. 5, the number density and the radial speed shown in panels (b) and (e) together with the location of the coronal current sheet shown by green color ($B_r=0$) in panel (a), we recognize that the flow speed (density) is lower (higher) in the neighborhood of the coronal current sheet and higher (lower) at the coronal hole, which is qualitatively in

agreement with the observed intensity pattern. In addition, we can observe the solar cycle variations, where the solar activity level increases, the high speed stream area reduces while the high density area changes reversely. During the solar minimum, the higher speed is confined to the poles and the low speed is near the equator, but the density varies almost inversely. These results are also consistent with the results in Fig. 5 of Hu et al. (2008), which were simulated by MHD models.

The solar wind speed at 1 AU is obtained by mapping the speed on the source surface of 2.5 Rs to that at the Earth's orbit through a linear relation: $v(1\ \mathrm{AU})=c_1\times v(2.5\ \mathrm{Rs})+c_2$, where

(1) $c_1=27.55$, $c_2=25$ at the solar maximum;
(2) $c_1=12.35$, $c_2=75$ at the descending and ascending phases;
(3) $c_1=9.15$, $c_2=155$ at the solar minimum.

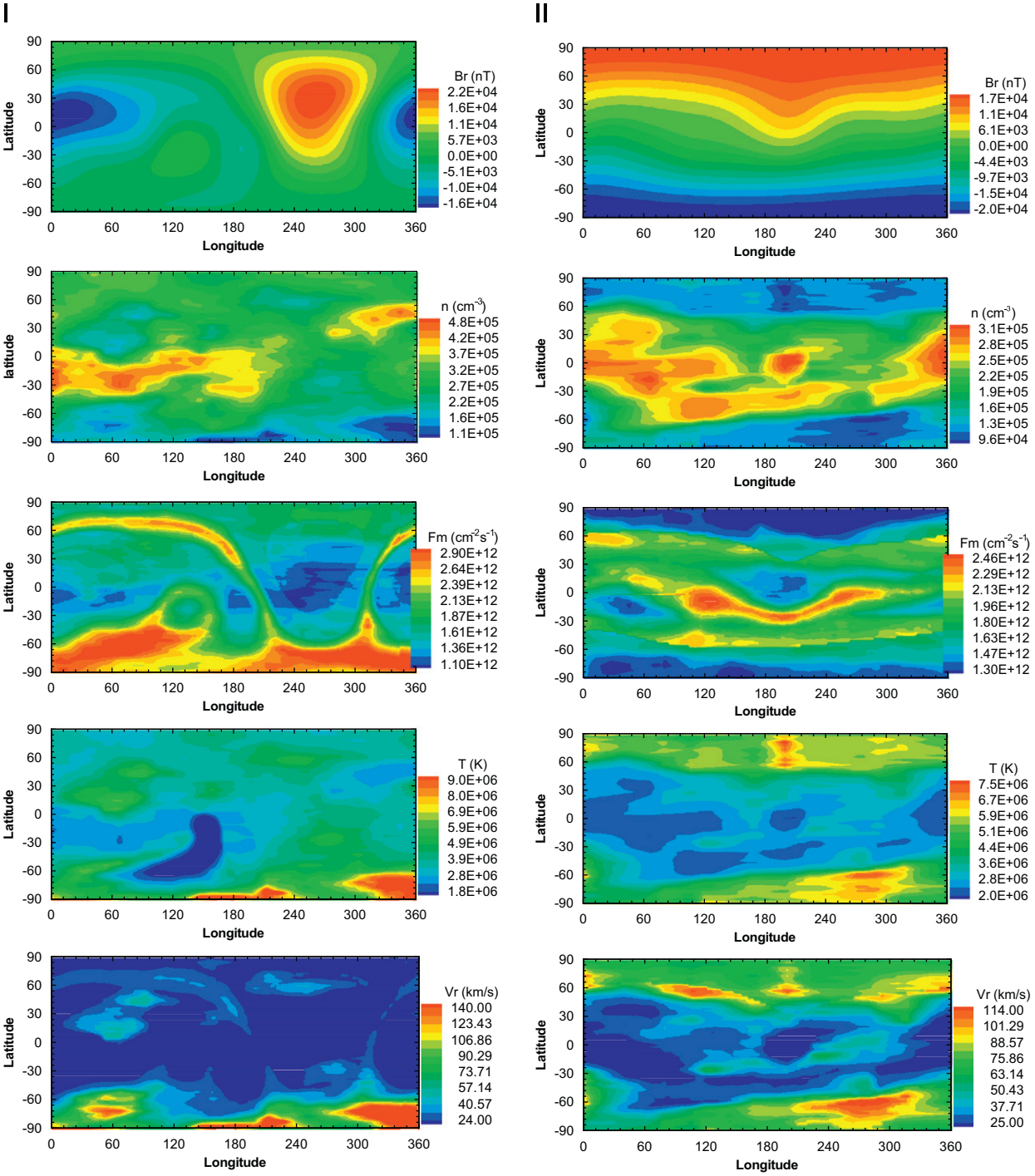

Fig. 5. Distribution of (a) the radial magnetic fields B_r and (b) the solar plasma number density n from observation; (c) the coronal mass output F_m, (d) the temperature and (e) the radial velocity on source surface of 2.5 Rs from numerical simulation at (i) CR 1823 in 1989 (maximum); (ii) CR 1874 in 1993 (descending phase); (iii) CR 1910 in 1996 (minimum); (iv) CR 1932 in 1998 (ascending phase).

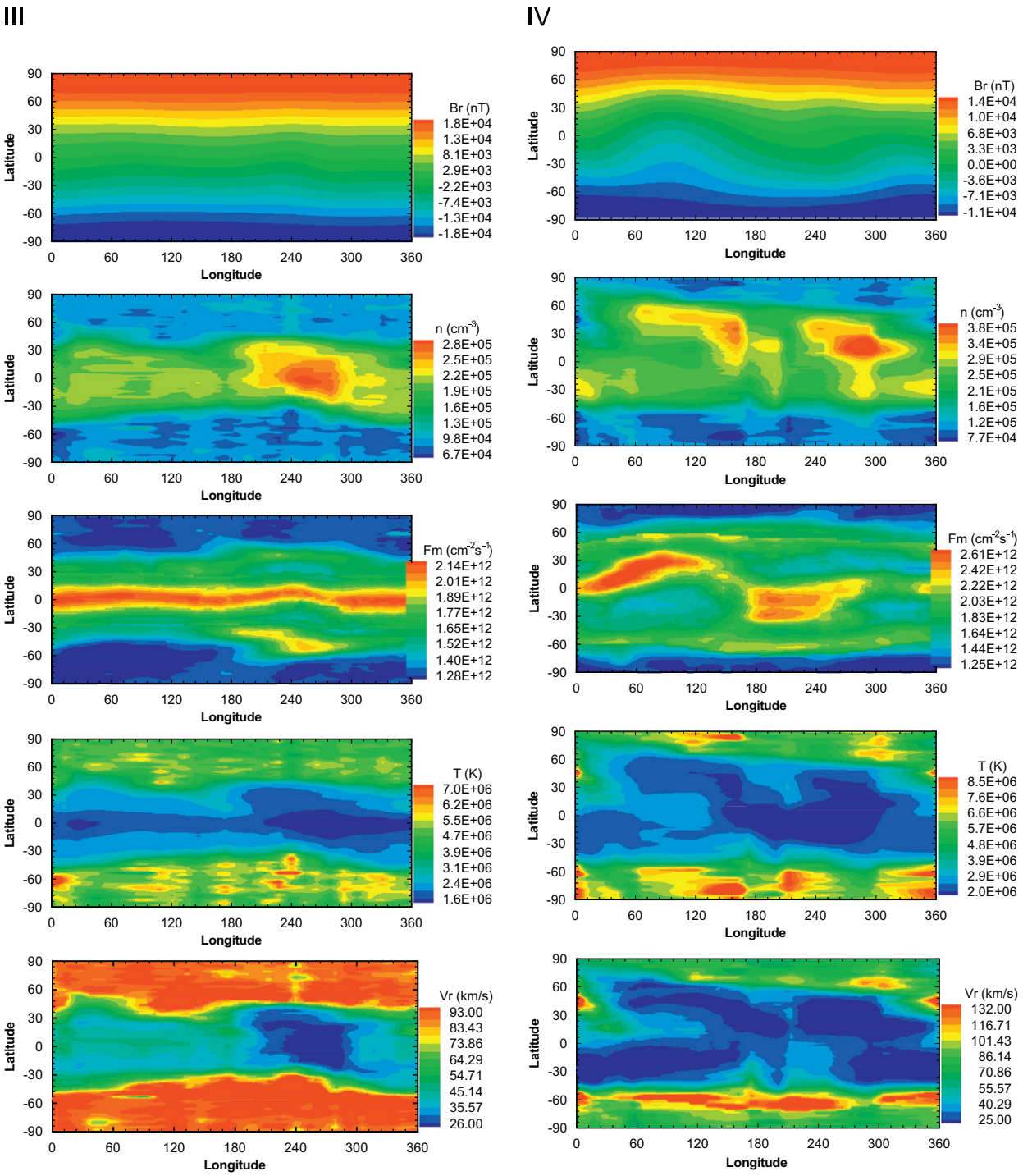

Fig. 5. (*Continued*)

The coefficients c_1 and c_2 are estimated by means of the radial speed relation of the solar wind given in the bottom panel of Fig. 7 by Withbroe (1988), which was also used by Wei et al. (2003) to give the solar wind speed at 1 AU. The black lines in panels (a)–(f) of Fig. 6 show the numerical speed at earth orbit during six time intervals: CRs 1821–1825 from 1989 to 1990 (a), which is at solar maximum, the whole 5 years: 1993 (b), 1995 (c), 1996 (d), 1997 (e) and 1998 (f), which goes through the descending phase ((b) and (c)), the solar minimum (most of the period of (d) and (e)) and the ascending phase ((f)). The WIND spacecraft observations (panels (c) to (f)) and IMP 8 (panels (a) and (b)) during the same time intervals as our simulation are given by red lines in Fig. 6. For comparison, the solar wind speeds at 1 AU simulated by the WSA model using expansion factor (f_s), which can be expressed as:

$v(f_s)=267.5+[410/(f_s)^{2/5}]$, where $f_s=(R_\odot/R_s)^2[B^p(R_\odot)/B^p(R_s)]$ is the magnetic expansion factor (Wang and Sheeley, 1990; Arge and Pizzo, 2000), are shown as blue lines during the same intervals as our simulation. The comparison of the numerical results of the solar wind speed with the observational results and the WSA model shows that their variations are qualitatively consistent during all the four phases of solar activity. In this context the self-consistent, global distributions on the source surface of 2.5 Rs during all the phases of a solar cycle can be used for understanding the change of the interplanetary condition.

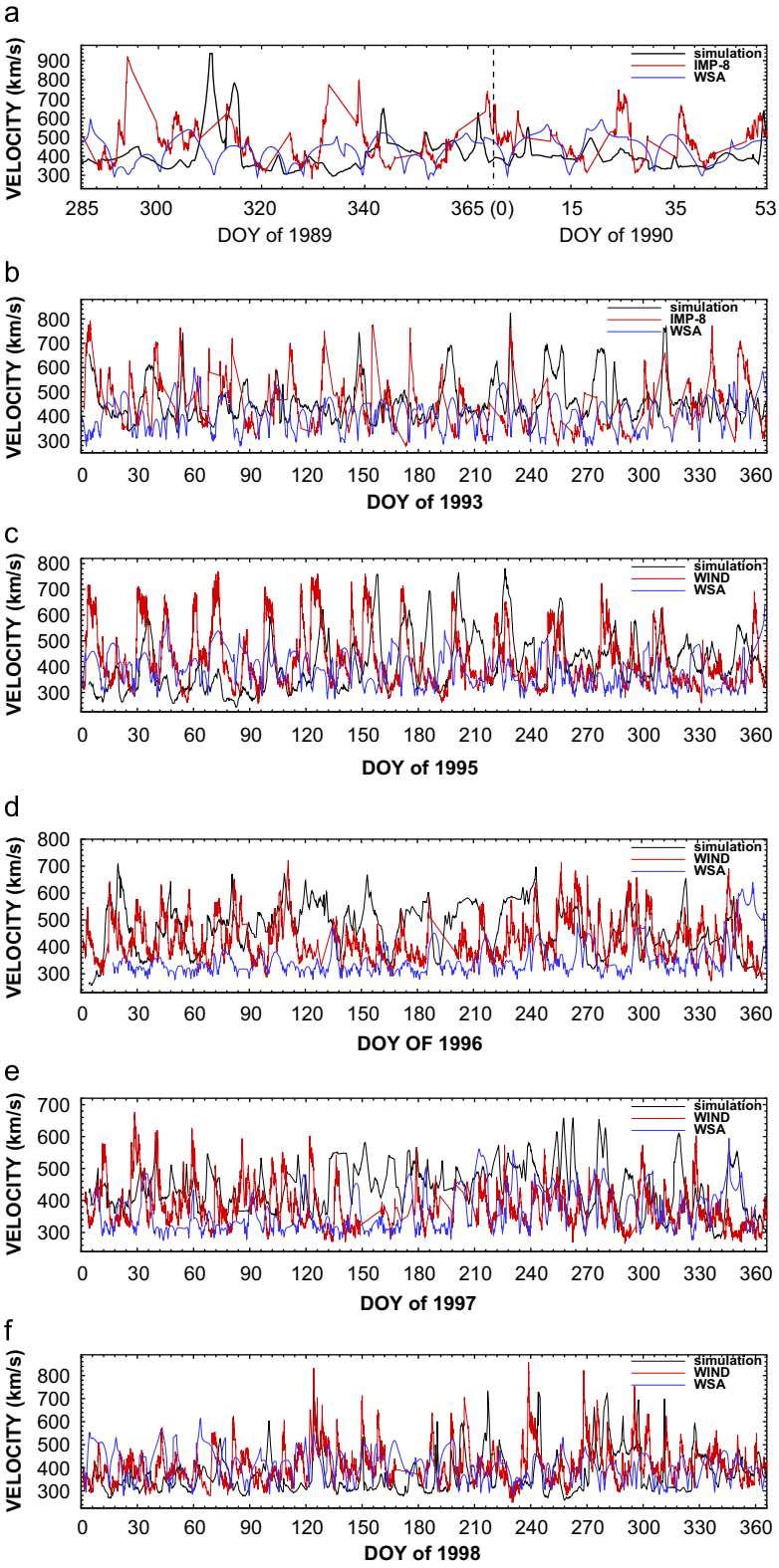

Fig. 6. Comparison of our simulated speed (black lines), the observational speed (red lines) and the simulated speed by WSA model (blue lines) at 1 AU during six time intervals: (a) CRs 1821–1825 of 1989 and 1990; (b) CRs 1864–1876 of 1993; (c) CRs 1891–1903 of 1995; (d) CRs 1904–1917 of 1996; (e) CRs 1918–1930 of 1997; and (f) CRs 1931–1944.

However, despite the qualitative similarity, the model results still have quantitative differences from the observations. In particular, the fast solar wind speed in the simulation at solar maximum is low compared to the measurements. The causes of the discrepancies between this simulation and the measurements and the WSA model may be twofold. On the one hand, the quantitative differences between the simulation results and the observations may be caused by the simple linear relation between

the speed at 2.5 Rs and 1 AU and the neglect of physical details near the Sun. On the other hand, the discrepancies may be also due to transient effects and interplanetary discontinuities (see, for example, Dryer, 1994 or Odstrcil et al., 2004), between 2.5 Rs and interplanetary space near 1 AU.

It is well known that solar wind MHD simulation is an initial-boundary value problem. The initial input to MHD simulation plays a crucial role in producing realistic solar wind background. Presently, an initial potential magnetic field derived from a photospheric field-based potential field and spherically symmetric Parker solar wind are popularly used as inputs. The self-consistent, time-dependent initial and boundary conditions, based on observational results, will be our ideal choice. But, no enough observational data can be used to constrain the MHD model. The aim of the present work is to provide a relative self-consistent initial-boundary value condition to the MHD model with more observational data considered. Our next goal is to use this more realistic, solar cycle dependent, self-consistent source surface model during all phases of the solar cycle as an inner-boundary condition for our MHD simulation. These preliminary works have made us believe that using such inner-boundary condition could helpfully improve the capability of 3D MHD models for the corona and heliosphere.

5. Conclusions

In this article, based on the observation results of the photospheric magnetic fields and K coronal brightness on the source surface of 2.5 Rs for 136 Carrington Rotations (CRs 1811–1946), a statistical analysis is made to obtain the average results of the magnetic field, the density and the coronal mass outputs flux pattern at 2.5 Rs. The CRs selected span the middle latter portion of solar cycle 22 (January 1989–April 1995) and the early portion of solar cycle 23 (May 1995–March 1999). They can be broadly grouped into four categories: solar maximum (CRs 1811–1825), the descending phase (CRs 1826–1904), solar minimum (CRs 1905–1925) and the ascending phase (CRs 1926–1946). Then, the statistical average results of magnetic field and density distribution are achieved separately during the four different phases. Fig. 2 illustrates how the magnetic structure and density distribution on the source surface of 2.5 Rs evolves during the course of the solar cycle. During the middle latter portion of solar cycle 22 and the early portion of solar cycle 23, the coronal current sheet at $r=2.5$ Rs can be approximately described as a tilted line relative to the solar equator in most times, with a tilt angle varying from $<20^\circ$ near minimum to $\sim 90^\circ$ at maximum (as also indicated on panel (a) of Fig. 5). Then, with the help of the velocity distribution model in the corona by Xiang et al. (2006), the distribution of the coronal mass outputs flux F_m is also analyzed statistically for the four different phases in Fig. 4.

Based on the statistical results of the magnetic field and density distribution and the statistical patterns of coronal mass outputs flux F_m, a numerical study of the global distribution near 2.5 Rs has been made by solving a self-consistent MHD system with different parameters during the four different phases. Four representative CRs in the four different phases are also chosen to numerically generate the solar-activity-dependent, self-consistent, global distributions of our source surface at 2.5 Rs. In Fig. 5, we can observe that the maximum and the minimum F_m are associated with different magnetic structures, the coronal current sheet and the polar corona region on the source surface. Meanwhile, the solar activity level variations can be also observed. When the solar activity level increases, (1) the correlation between the maximum (minimum) F_m and the coronal current sheet region (polar corona region) becomes more and more irregular; (2) the high speed stream spreads to the lower latitude while the density changes reversely. During the solar minimum, (1) a good correlation exists between the maximum F_m and the coronal current sheet patterns; (2) the higher speed is confined to the poles and a low speed is near the equator, but the density varies almost inversely.

The solar wind speed at 1 AU is obtained by mapping the speed on the source surface of 2.5 Rs to that at 1 AU during more than 5 years and covering the four different phases of solar activity, which lead to a more quantitative low-boundary condition that can be used in numerical models of space weather events. The comparison of the numerical results with the observational results by the WIND spacecraft and the simulation result of the WSA model shows that their variations are qualitatively consistent in speed in the different phases of solar activity. It indicates that the global distributions on the source surface of 2.5 Rs during all phases of the solar cycle could be used to predict the changes in the interplanetary medium. While the model results still have quantitative differences from the observations, but it may be caused by the simple linear relation between the speed at 2.5 Rs and 1 AU and physical details near the Sun that are not considered here. The dynamic processes, due to transient effects (Dryer, 1994; Odstrcil et al., 2004), between 2.5 Rs and interplanetary space near 1 AU are not taken into consideration.

In summary, based on certain regular coronal mass outputs flux F_m and the observation results of the magnetic field and density on the source surface, the statistical and numerical study of the global distribution near 2.5 Rs during all phases of solar activity will provide solar cycle dependent, self-consistent inner-boundary and initial boundary. These can improve the capability of a 3D MHD model for predicting the changes in interplanetary space.

Acknowledgements

The contours of K corona white light brightness at 1.36 Rs are obtained from the High Altitude Observatory (HAO), solar photospheric magnetic field data are from the Wilcox Solar Observatory (WSO), and solar wind speeds at 1 AU are taken from the observation data of the WIND spacecraft and IMP 8 satellite. This work is jointly supported by the National Natural Science Foundation of China (40921063, 40874077, 40890162 and 40874091), the 973 project under grant 2006CB806304, and the Specialized Research Fund for State Key Laboratories.

References

Arge, C.N., Pizzo, V.J., 2000. Improvement in the prediction of solar wind conditions using near-real time solar magnetic field update. Journal of Geophysical Research 105 (A5), 10,465–10,479.
Dryer, M., 1994. Interplanetary studies: propagation of disturbances between the Sun and the magnetosphere. Space Science Review 67, 363–419.
Feng, X.S., Zhao, X.H., 2006. Geoeffective analysis of CMEs under current sheet magnetic coordinates. Astrophysics Space Science 111, A09108.
Feng, X., et al., 2005. A comparative study on 3-D solar wind structure observed by Ulysses and MHD simulation. Chinese Science Bulletin 50 (7), 672–678.
Fisk, L.A., 2001. On the global structure of the heliospheric magnetic field. Journal of Geophysical Research 106 (A8), 15,849–15,857.
Gary, G.A., 2001. Plasma beta above a solar active region: rethinking the paradigm. Solar Physics 203, 71–86.
Grall, R.R., Coles, W.A., Klinglesmith, M.T., et al., 1996. Rapid acceleration of the polar solar wind. Nature 379, 429–432.
Guhathakurta, M., Holzer, T.E., MacQueen, R.M., 1996. The large-scale density structure of the solar corona and the heliospheric current sheet. The Astrophysical Journal 459, 817–831.
Guo, W.P., Wu, S.T, 1998. A magnetohydrodynamic description of coronal helmet streamers containing a cavity. The Astrophysical Journal 494, 419–429.
Harvey, K.L., White, O.R., 1999. What is solar cycle minimum? Journal of Geophysical Research 104 (A9) 19,759–19,764.

Hu, Y., Feng, X., Wu, S.T., Song, W., 2008. Three-dimensional MHD modeling of the global corona throughout solar cycle 23. Journal of Geophysical Research 113, A03106.

Lallement, R., Holzer, T.E., Mumro, R.H., 1986. Solar wind expansion in a polar coronal hole: inferences from coronal white light and interplanetary Lyman alpha observations. Journal of Geophysical Research 91 (A6), 6751–6759.

Leinert, C., Jackson, B.V., 1998. Global solar wind changes over solar cycle 21: a combination of Helios photometer, in situ, and interplanetary scintillation data. The Astrophysical Journal 505, 984–992.

Liewer, P.C., Hall, J.R., De Jong, M., Socker, D.G., Howard, R.A., Crane, P.C., Reiser, P., Rich, N., Vourlidas, A., 2001. Determination of three dimensional structure of coronal streamers and relationship to the solar magnetic field. Journal of Geophysical Research 106 (A8), 15,903–15,915.

Linker, J.A., Mikic, Z., Bisecker, D.A., Forsyth, R.J., Gibson, S.E., Lazarus, A.J., Lecinski, A., Riley, P., Szabo, A., Thompson, B.J., 1999. Magnetohydrodynamic modeling of the solar corona during whole Sun month. Journal of Geophysical Research 104 (A5), 9809–9830.

Luhmann, J.G., Li, Y., Arge, C.N., Gazis, P.R., Ulrich, R., 2002. Solar cycle changes in coronal holes and space weather cycles. Journal of Geophysical Research 107 (A8), 1154. doi:10.1029/2001JA007550.

McComas, D.J., Elliott, H.A., Schwadron, N.A., et al., 2003. The three dimensional solar wind around solar maximum. Geophysical Research Letters 30 (10), 1517–1520.

Mullan, D.J., 1983. Momentum flux invariance in the solar wind. The Astrophysical Journal 272, 325–328.

Neugebauer, M., et al., 1998. Spatial structure of the solar wind and comparisons with solar data and models. Journal of Geophysical Research 103 (A7), 14,587–14,599.

Oliver, R., Ballester, J.L., 1995. Short-term periodicities in sunspot areas during solar cycle 22. Solar Physics 156, 145–155.

Odstrcil, D., Pizzo, V.J., Linker, J.A., et al., 2004. Initial coupling of coronal and heliospheric numerical magnetohydrodynamic codes. Journal of Atmospheric and Solar Terrestrial Physics 66, 1311–1320.

Owens, M.J., Spence, H.E., Mcgregor, S., et al., 2008. Metrics for solar wind prediction models: comparison of empirical, hybrid, and physics based schemes with 8 years of L1 observations. Space Weather, 6. doi:10.1029/2007SW000380.

Parker, E.N., 1963. Interplanetary Dynamical Processes. Wiley-Interscience, New York.

Pätzold, M., Tsurutani, B.T., Bird, M.K., 1997. An estimate of large-scale solar wind density and velocity profiles on a coronal hole and the coronal streamer belt. Journal of Geophysical Research 102, 24,151–24,160.

Phillips, J.L., Bames, S.J., Feldman, W.C., et al., 1995. Ulysses solar wind plasma observations at high southerly latitudes. Science 268, 1030–1033.

Priest, E.R., et al., 1998. Nature of the heating mechanism for the diffuse corona. Nature 393, 545.

Riley, P., Linker, J.A., Mikic, Z., Lionello, R., Ledvina, S.A., Luhmann, J.G., 2006. A comparison between global solar magnetohydrodynamic and potential field source surface model results. The Astrophysical Journal 653, 1510–1516.

Riley, P., Linker, J.A., Mikic, Z., 2001. An empirically driven global MHD model of the solar corona and inner heliosphere. Journal of Geophysical Research 106 (A8), 15,889–15,901.

Scholl, I.F., Habbal, S.R., 2008. Automatic detection and classification of coronal holes and filaments based on EUV and magnetogram observations of the solar disk. Solar Physics 248 (2), 425–439.

Shen, F., Feng, X., Wu, S.T., Xiang, C., 2007. Three-dimensional MHD simulation of CMEs in three-dimensional background solar wind with the self-consistent structure on the source surface as input: numerical simulation of the January 1997 Sun–Earth connection event. Journal of Geophysical Research 112, A06109.

Smith, E.J., 2001. The heliospheric current sheet. Journal of Geophysical Research 106 (A8), 15,819–15,831.

Steinitz, R., Eyni, M., 1980. Global properties of the solar wind I. The invariance of the momentum flux density. The Astrophysical Journal 241, 417–424.

Suess, S.T., Wang, A.-H., Wu, S.T., 1996. Volumetric heating in coronal streamers. Journal of Geophysical Research 101 (A9), 19,957–19,966.

Svalgaard, L., 2006. How good (or bad) are the inner boundary conditions for heliospheric solar wind modeling. SHINE 2006 Workshop, Zermatt, Utah, 31 July–4 August, 2006.

Svalgaard, L., Duvall Jr., T.L., Scherrer, P.H., 1978. The strength of the suns polar fields. Solar Physics 58, 225–239.

Toma, G.D., White, O.R., Harvey, K.L., 2000. A picture of solar minimum and the onset of solar cycle 23. I. Global magnetic field evolution. The Astrophysical Journal 529, 1101–1114.

Wang, A.-H., Wu, S.T., Suess, S.T., Poletto, G., 1998. Global model of the corona with heat and momentum addition. Journal of Geophysical Research 103 (A2), 1,913–1,922.

Wang, Y.M., Sheeley Jr., N.R., 1990. Solar wind speed and coronal flux tube expansion. The Astrophysical Journal 355, 726–732.

Wang, Y.M., Sheeley Jr., N.R., 1992. On potential field models of the solar corona. The Astrophysical Journal 392, 310–319.

Wei, F.S., Feng, X.S., Cai, H.C., Zhou, Q.J., 2003. Global distribution of coronal mass outputs and its relation to solar magnetic field sturctures. Journal of Geophysical Research 108 (A6), 1238. doi:10.1029/2002JA009439.

Withbroe, G.L., 1988. The temperature structure, mass and energy flow in the corona and inner solar wind. The Astrophysical Journal 325, 442–467.

Withbroe, G.L., Kohl, J.L., Weiser, H., Munro, R.H., 1985. Coronal temperatures, heating, and energy flow in a polar region of the sun at solar maximum. The Astrophysical Journal 297, 324–337.

Xiang, C.Q., Feng, X.S., Fan, Q.L., Yao, J.S ., 2006. An observation-based model of solar wind background. Chinese Journal of Space Science 26 (3), 161–166.

Zhao, X.P., Hoeksema, J.T., 1994. A coronal magnetic field model with horizontal volume and sheet current. Solar Physics 151, 91–105.